

RESEARCH ARTICLE Topographic form stress in the Southern Ocean State Estimate

10.1002/2015JC011143

Jessica Masich¹, Teresa K. Chereskin¹, and Matthew R. Mazloff¹

Key Points:

- Topographic form stress balances 95% of Southern Ocean wind stress
- Shallow form stress in the top 3700 m balances most of the wind stress
- Approximately 40% of wind stress is balanced by form stress across land, 60% by submerged ridges

Correspondence to:

J. Masich,
jemillar@ucsd.edu

Citation:

Masich, J., T. K. Chereskin, and M. R. Mazloff (2015), Topographic form stress in the Southern Ocean State Estimate, *J. Geophys. Res. Oceans*, 120, 7919–7933, doi:10.1002/2015JC011143.

Received 15 JUL 2015

Accepted 9 NOV 2015

Accepted article online 12 NOV 2015

Published online 17 DEC 2015

¹Scripps Institution of Oceanography, University of California San Diego, San Diego, California, USA

Abstract We diagnose the Southern Ocean momentum balance in a 6 year, eddy-permitting state estimate of the Southern Ocean. We find that 95% of the zonal momentum input via wind stress at the surface is balanced by topographic form stress across ocean ridges, while the remaining 5% is balanced via bottom friction and momentum flux divergences at the northern and southern boundaries of the analysis domain. While the time-mean zonal wind stress field exhibits a relatively uniform spatial distribution, time-mean topographic form stress concentrates at shallow ridges and across the continents that lie within the Antarctic Circumpolar Current (ACC) latitudes; nearly 40% of topographic form stress occurs across South America, while the remaining 60% occurs across the major submerged ridges that underlie the ACC. Topographic form stress can be divided into shallow and deep regimes: the shallow regime contributes most of the westward form stress that serves as a momentum sink for the ACC system, while the deep regime consists of strong eastward and westward form stresses that largely cancel in the zonal integral. The time-varying form stress signal, integrated longitudinally and over the ACC latitudes, tracks closely with the wind stress signal integrated over the same domain; at zero lag, 88% of the variance in the 6 year form stress time series can be explained by the wind stress signal, suggesting that changes in the integrated wind stress signal are communicated via rapid barotropic response down to the level of bottom topography.

1. Introduction

Strong, persistent winds over the Southern Ocean drive the Antarctic Circumpolar Current (ACC) on an unblocked eastward path around Antarctica. In a closed ocean basin, continental barriers support a western boundary current structure that balances the momentum input by wind stress; lacking any zonal bounds, the ACC must balance wind stress via other means. While momentum input into the Southern Ocean can be estimated via satellite observations of surface winds, mechanisms for how momentum exits the system are more difficult to observe. Observations and reanalyses have shown an increase in the strength of Southern Ocean wind stress [Thompson and Solomon, 2002; Swart and Fyfe, 2012], while the ACC baroclinic transport appears to remain stable [Böning et al., 2008], suggesting that the interior mechanisms that remove momentum from the ACC system are counterbalancing changes in the input wind stress. Here we describe where and how momentum exits the ACC system in the Southern Ocean State Estimate (SOSE) model.

Munk and Palmén [1951] first proposed a momentum sink, uniquely important in the Southern Ocean, which might serve to balance the wind stress: form stress across bottom topography. Munk and Palmén estimated that the four tallest ridges under the ACC—the Kerguelen Plateau, Macquarie Ridge, Scotian Arc, and East Pacific Rise—could provide enough zonal pressure gradient across each ridge to balance the wind stress in the zonal mean. We evaluate Munk and Palmén's conjecture by mapping all momentum sources and sinks in the SOSE Southern Ocean between 30°S and 77°S; these maps confirm the broad strokes of their theory but reveal a more complex structure.

2. Background

The Southern Ocean State Estimate (SOSE) is a 1/6°, eddy-permitting model of the Southern Ocean. Based on the MITgcm, SOSE employs an iterative adjoint method to perform a least squares fit to observational data from myriad sources, including satellite altimetry and sea surface temperature observations, CTD data from the Argo program and various other observational programs, and bottom pressure and acoustic travel time data from Inverted Echo Sounder experiments. SOSE is constrained by the 1° Ocean Comprehensible

Atlas (OCCA) world ocean state estimate at its northern boundary at 24.7°S, and by European Center for Medium-Range Weather Forecast reanalysis interim atmospheric model data at the ocean surface [Mazloff *et al.*, 2010]. Bottom topography in the SOSE model comes from Smith and Sandwell and the Earth Topography Five-Minute Grid; these data sets are binned to a 1/4° resolution, and then interpolated to the 1/6° SOSE grid (Figure 6a). The model has 42 depth levels, with resolution ranging from 10 m at the surface to 250 m at depth. Overall, the SOSE model represents the observed Southern Ocean reasonably well; the 2005–2006 solution better represented the observational data available during that time than did the World Ocean Atlas 2001 climatology [Mazloff *et al.*, 2010]. The current model run, spanning 2005 through 2010, assimilates more observational data than this 2005–2006 solution. SOSE’s unique combination of eddy-permitting model physics with observational data represents the best possible guess at otherwise unobservable Southern Ocean characteristics, including the basin-scale topographic form stress signal.

The zonally and vertically integrated zonal momentum equation reduces to four terms (see Appendix A):

$$\rho_0 \oint_x \frac{\partial}{\partial y} \int_{z=-H}^{\eta} \overline{uv} dz dx = - \oint_x \int_{z=-H}^{\eta} \frac{\partial \overline{p}}{\partial x} dz dx + \oint_x \overline{\tau_{wind}^x} dx - \oint_x \overline{\tau_{friction}^x} dx, \quad (1)$$

where the overbars denote the time mean, ρ_0 is background seawater density, η is the sea surface height, $-H$ is the depth at the seafloor, u is zonal velocity, v is meridional velocity, p is pressure, τ_{wind}^x is zonal wind stress at the surface, and $\tau_{friction}^x$ is zonal stress due to bottom and sidewall friction.

The four terms in equation (1)—from left, meridional momentum flux divergence, topographic form stress contained within the pressure gradient term, wind stress, and bottom friction—form the primary ACC balance in the zonal and depth integral. Eastward momentum from wind stress is the main source of momentum sustaining the ACC, but all three remaining terms can contribute to the westward momentum that balances this term.

Time-mean depth-integrated fields of each term in equation (1) give us an initial sense of what terms may be most important in the momentum balance (Figure 1); while the bottom friction, wind stress, and flux divergence terms are of the same magnitude, the zonal pressure gradient term is an order of magnitude larger. Flux divergence, bottom friction, and pressure gradient fields change sign frequently throughout the domain, while wind stress remains steadily positive over most of the Southern Ocean; thus in the zonal integral, we can expect the wind stress to be large while the bottom friction and advection terms will be smaller. The subset of the pressure gradient field that involves pressure gradients across topography (water leaning on land) is overwhelmed by the pressure gradients in the ocean interior (water leaning on water), but only the pressure gradients across topography contribute to the zonally integrated momentum balance. Extraction of the topographic form stress field from the total zonal pressure gradient field is described in section 3.

Previous numerical studies have confirmed that in the zonal integral, wind stress is primarily balanced by topographic form stress. *McWilliams et al.* [1978], *Treguier and McWilliams* [1990], *Wolff et al.* [1991], and *Marshall et al.* [1993] have shown that topographic form stress balances wind stress in simple two-layer and three-layer quasi-geostrophic channel models. More recently, *Ward and Hogg* [2011] used a five-layer rotating wind-driven channel model to show that while bottom friction and northward transport tend to balance wind stress during spin-up, topographic form stress balances wind stress once the model reaches equilibrium. *Howard et al.* [2015] used a similar three-layer channel model, this time with both buoyancy forcing and wind forcing, to show that while bottom friction balances the buoyancy forcing at equilibrium, it is topographic form stress that balances the wind stress forcing.

The zonal integral has also been explored in high resolution general circulation models as well; in the 1/2° by 1/4°, 32-level Fine Resolution Antarctic Model (FRAM), topographic form stress was shown to balance wind stress in the zonal average in the unblocked latitudes by *Killworth and Nanneh* [1994] and *Stevens and Ivchenko* [1997], and along streamlines in the ACC latitudes by *Ivchenko et al.* [1996]. *Grezio et al.* [2005] showed that topographic form stress balances wind stress in the zonal mean in both the 1/4°, 36-level OCCAM project model and the 20-level Parallel Ocean Program (POP) model as well, with a small but significant contribution from eddy flux divergence in both models.

To our knowledge, only *Gille* [1997] has investigated the zonal structure of the topographic form stress signal in a model with realistic topography. Using the 0.4°, 20-level Semptner-Chervin model for latitudes

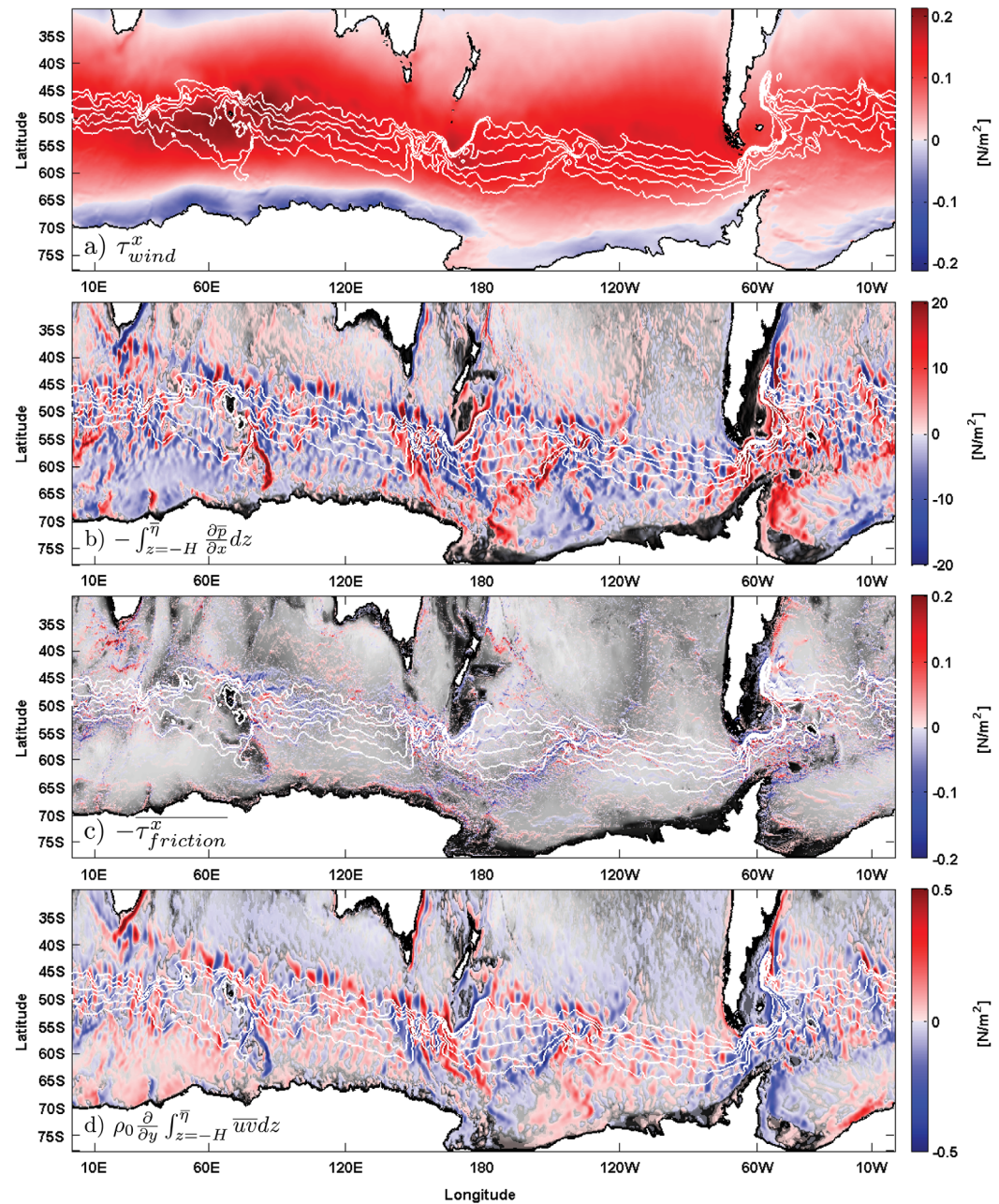


Figure 1. Vertically integrated 6 year time-mean momentum balance terms: (a) wind stress; (b) vertically integrated zonal pressure gradient; (c) bottom and sidewall friction; (d) meridional momentum flux divergence. White lines show SOSE ACC streamlines.

spanning 30°S to 70°S, Gille [1997] found that topographic form stress balanced wind stress at all latitudes in the domain.

Gille [1997] approached the difficult problem of extracting the topographic form stress signal from the full zonal pressure gradient field by dividing the ACC longitudinally into 10° sectors, and taking the difference between the geostrophic transport that would be driven by the zonal pressure gradient across the sector and the actual geostrophic transport observed through the sector. The residual between the two signals was attributed to a pressure gradient across topography in the sector, and Gille [1997] was able to show that topographic form stress acts as a momentum sink primarily at three locations along the ACC: Kerguelen and Campbell Plateaus, and the Drake Passage. The results using this method, however, are sensitive to the

choice of longitudinal sectors, and may neglect contributions to the form stress signal that come from pressure gradients across topography that is wider than the 10° sector size.

Using the observationally constrained SOSE model from 30°S to 77°S, we take a more direct approach, calculating the pressure gradient across every piece of topography in the domain rather than taking longitudinal sections. We find that in the ACC latitudes 42°S to 65°S, 95% of the net integrated zonal wind stress is balanced by topographic form stress, while meridional momentum flux divergence and bottom/sidewall friction together contribute only 5% of the westward momentum balance needed to balance the wind stress. Our results align with previous studies in that topographic form stress serves as the primary balance for wind stress, but our analysis reveals a complex structure for the topographic form stress field.

3. Methods

The zonal-integrated and depth-integrated total zonal pressure gradient term can be written:

$$-\oint_x \int_{z=-H}^{\bar{\eta}} \frac{\partial \bar{p}}{\partial x} dz dx = - \underbrace{\oint_x \frac{\partial}{\partial x} \int_{z=-H}^{\bar{\eta}} \bar{p} dz dx}_i + \underbrace{\oint_x \bar{p}_{atm} \frac{\partial \bar{\eta}}{\partial x} dx}_{ii} + \underbrace{\oint_x \bar{p}_b \frac{\partial H}{\partial x} dx}_{iii}, \quad (2)$$

where $p_{atm} = p(z = \eta)$ is the atmospheric pressure at the surface, and $p_b = p(z = -H)$ is the bottom pressure at the seafloor. Term (i) in this equation is the net pressure gradient across a zonally bounded basin; *Olbers* [1998] notes that in a closed, flat-bottomed basin, this term alone would balance input wind stress over the basin. In the unblocked latitudes, term (i) vanishes, and term (ii) and term (iii) represent the transfer of zonal momentum from the atmosphere to the fluid via form stress and from the fluid to the solid earth via form stress, respectively. Term (ii) in this domain is negligibly small, but in the blocked latitudes, both term (i) and term (iii) contribute to the total form stress signal by denoting the transfer of zonal momentum from the fluid to the earth at the continental boundaries.

To capture all three contributions to the total form stress signal in the numerical model, we discretize the left-hand side of equation (2):

$$-\oint_x \int_{z=-H}^{\bar{\eta}} \frac{\partial \bar{p}}{\partial x} dz dx = - \sum_x \sum_z \frac{\Delta \bar{p}}{\Delta x} \Delta z \Delta x = - \sum_x \sum_z \Delta \bar{p} \Delta z. \quad (3)$$

This term will reveal the topographic form stress signal, since only momentum transferred to the solid earth will remain in the full circumpolar integral. We refine this calculation in order to locate where these transfers occur.

To extract the topographic form stress signal from the overall pressure field, we first isolate all points in the 3-D SOSE pressure field that lie adjacent to topography, $p_b = p(z = -H)$. Though SOSE employs partial cells, in which a fraction of the cell contains fluid and a fraction contains land, we simplify the topographic field so that Δz in this methodology is simply the height of the cell itself, which results in a small uncertainty (2% average, 5.2% maximum) in the integration depth over which the form stress is distributed. For every z -level and along every x -line on the SOSE grid that transects a given region of topography—a seamount, for instance—we calculate the form stress signal by first taking the pressure difference, east-minus-west, between the ocean cell adjacent to the eastern face of the seamount and the ocean cell adjacent to the western face (Figure 2a):

$$\Delta \bar{p}_b = \bar{p}_b(x = x_E) - \bar{p}_b(x = x_W). \quad (4)$$

For all plots of the form stress field, we divide the pressure difference $\Delta \bar{p}_b$ by the width of the seamount Δx over which the pressure difference occurs (Figure 2b):

$$\frac{\Delta \bar{p}_b}{\Delta x} = \frac{\bar{p}_b(x = x_E) - \bar{p}_b(x = x_W)}{x_E - x_W}. \quad (5)$$

We vertically integrate these topographic pressure gradients to show the vertically integrated pressure gradient fields shown in Figures 2c, 4, and 7:

$$\sum_{z=-H}^{\bar{\eta}} \frac{\Delta \bar{p}_b}{\Delta x} \Delta z, \quad (6)$$

and we zonally integrate to find the total form stress signal:

$$-\oint_x \int_{z=-H}^{\bar{\eta}} \frac{\partial \bar{p}}{\partial x} dz dx = \sum_{\text{ridges } z=-H}^{\bar{\eta}} \frac{\Delta \bar{p}_b}{\Delta x} \Delta z \Delta x = \sum_{\text{ridges } z=-H}^{\bar{\eta}} \Delta \bar{p}_b \Delta z, \quad (7)$$

where we have adopted *Olbers et al.'s* [2004] use of “ridges” to denote both landmasses and submerged topography. The sign changes here because $\Delta \bar{p}_b$ is calculated across topography, rather than across the ocean basin bound by that topography. Only pressure differences across topography are included in the form stress signal, but every piece of topography—from small seamounts to continents to plains separating abyssal basins—is included in the calculation of the signal.

Finally, we note that in a flat-bottomed periodic ocean, the total pressure gradient $\partial p / \partial x$ must be zero when integrated zonally:

$$\oint_x \frac{\partial \bar{p}}{\partial x} dx = 0. \quad (8)$$

In a periodic ocean interrupted by ridges, the zonally integrated total pressure gradient will be the sum of the pressure differences across those ridges, with opposite sign:

$$\oint_x \frac{\partial \bar{p}}{\partial x} dx = - \sum_{\text{ridges}} \Delta \bar{p}_b. \quad (9)$$

We use this relationship to confirm our methodology by comparing the zonally integrated topographic form stress calculation to the zonal integral of the total pressure gradient. We find that the two integrated fields are indeed identical in magnitude, with opposite sign, at every latitude and every depth in the domain.

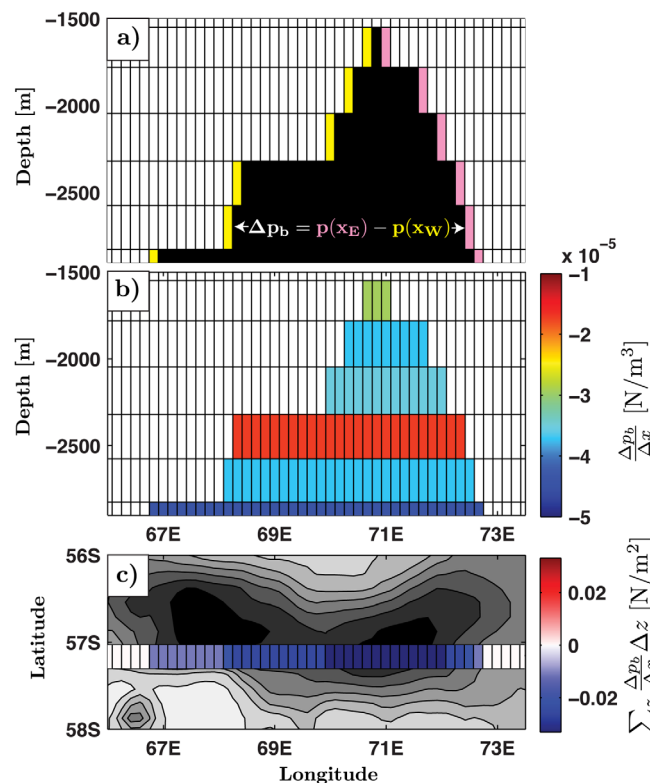


Figure 2. (a) Consider a zonal slice through a seamount south of Kerguelen Plateau: white cells indicate areas that contain water, black cells indicate areas that contain land. Pressure on the westward flank (yellow) is subtracted from the pressure on the eastward flank (pink). (b) The pressure difference is divided by the width of the seamount that separates the cells, and this pressure gradient $\Delta p_b / \Delta x$ is assigned to each z-level on the seamount. (c) Pressure gradients at each vertical level are integrated vertically to calculate the form stress field. Zonally integrating this field yields the total vertically and zonally integrated form stress signal.

The two integrated fields are indeed identical in magnitude, with opposite sign, at every latitude and every depth in the domain.

4. Results

4.1. Time-Mean Momentum Balance

In the 6 year SOSE mean, the total xy-integrated zonal wind stress is almost entirely balanced by topographic form stress. For the latitudes that border the northern and southernmost closed ACC transport streamlines, 42°S to 65°S, the time-mean total integrated eastward wind stress for the 6 year SOSE run is 6.67×10^{12} N (Table 1). Total integrated topographic form stress contributes 6.36×10^{12} N net westward momentum (balancing 95% of the total wind stress); bottom and sidewall friction contributes 1.9×10^{11} N net westward momentum (balancing 3% of the wind stress); and momentum flux divergences at the meridional boundaries account for 1.6×10^{11} N net westward momentum (2%).

For the full domain 30°S to 77°S, these numbers are slightly different (Table 1). While the total integrated eastward wind stress is 8.03×10^{12} N, the total

Table 1. xyz-Integrated Momentum Terms^a

y Domain	Wind Stress	Topographic Form Stress	Frictional Stress	Flux Divergence
ACC latitudes 42°S to 65°S	6.67×10^{12} N (+100%)	-6.36×10^{12} N (-95%)	-0.19×10^{12} N (-3%)	-0.16×10^{12} N (-2%)
Full domain 30°S to 77°S	8.03×10^{12} N (+100%)	-7.30×10^{12} N (-91%)	-0.11×10^{12} N (-1%)	-0.61×10^{12} N (-8%)

^aPositive sign indicates eastward direction; negative sign indicates westward direction.

integrated westward topographic form stress is 7.30×10^{12} N (balancing 91% of the wind stress); bottom friction is 1.1×10^{11} N (balancing 1%); and momentum flux divergence across the 30°S boundary accounts for 6.1×10^{11} N (balancing 8%). Figure 3 shows that the zonally integrated topographic form stress not only balances wind stress in the total integral, but at every latitude as well.

When we move out of the zonally integrated regime, the horizontal structure of the wind stress and topographic form stress fields diverge radically. Figure 4a shows the topographic form stress signal integrated over the full ocean depth. While the wind stress signal (Figure 1a) exhibits relatively little horizontal variation, the topographic form stress signal varies in both magnitude and sign.

Within the ACC latitudes, the most readily understood form stress signal is the strong westward (Figure 4a, blue) form stress that concentrates over South America and the ridges that underlie the ACC—Kerguelen Plateau, the Southeast Indian Ridge, the Macquarie Ridge region, the southernmost portion of the East Pacific Rise, and the Phoenix and Shackleton Fracture Zones in the Drake Passage. More surprising is the presence of eastward (Figure 4a, red) form stress in the field, due to higher pressure on the east flank of topography than on the west flank. These positive zonal pressure gradients are perhaps less intuitive, since they imply an acceleration of the eastward ACC flow. Eastward topographic form stress in the ACC is not without precedent; *Holloway* [1987] noted that form stresses could act in the same direction as the mean

flow in a simple QG model, and both *Stevens and Ivchenko* [1997] and *Grezio et al.* [2005], found in general circulation models that the deepest zonally integrated topographic form stress signals, though an order of magnitude smaller than the wind stress, acted eastward rather than westward. We attribute this net eastward deep form stress to pressure differences across the deepest ocean basins, discussed in section 4.3.

South and north of the ACC latitudes, the topographic form stress signals have less to do with ACC dynamics. South of the ACC latitudes, pressure differences between the subpolar gyres dominate the topographic form stress signal. Higher pressure in the eastern Weddell Sea than in the western Amundsen, Bellingshausen, and Ross Seas causes a positive zonal pressure gradient across the Antarctic Peninsula, and a corresponding negative pressure gradient (Figure 4a, blue) across the rest of the Antarctic continent that separates them.

North of the ACC latitudes, pressure differences between the subtropical gyres similarly dominate the form stress signal. A positive zonal pressure gradient between the Indian and Pacific gyres and

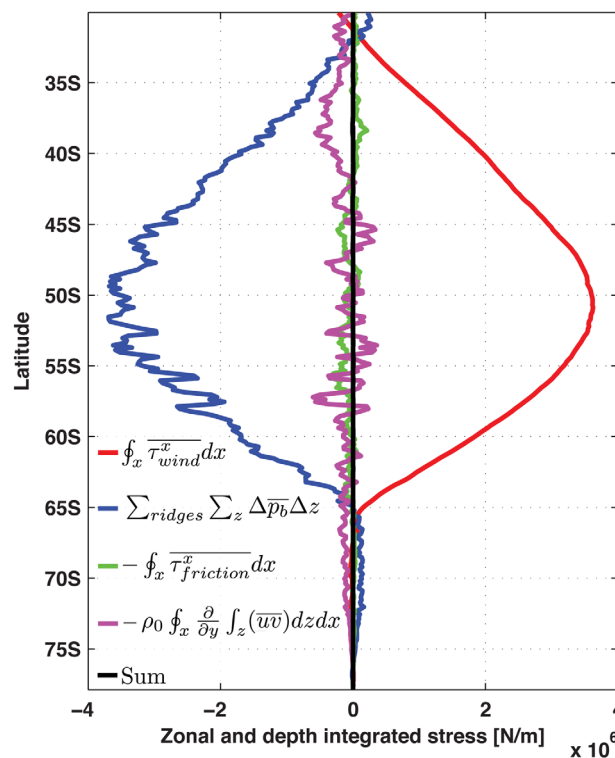


Figure 3. Zonal and depth-integrated stress terms between 30°S and 77°S. Integrated bottom and sidewall friction (green) and momentum flux divergence (magenta) terms are relatively small at all latitudes. Integrated wind stress (red) is large between 32°S and 65°S, and integrated topographic form stress (blue) is similarly large at these latitudes, balancing wind stress. The black line shows the sum of these terms, demonstrating that these four terms encompass the full zonal and depth-integrated momentum balance.

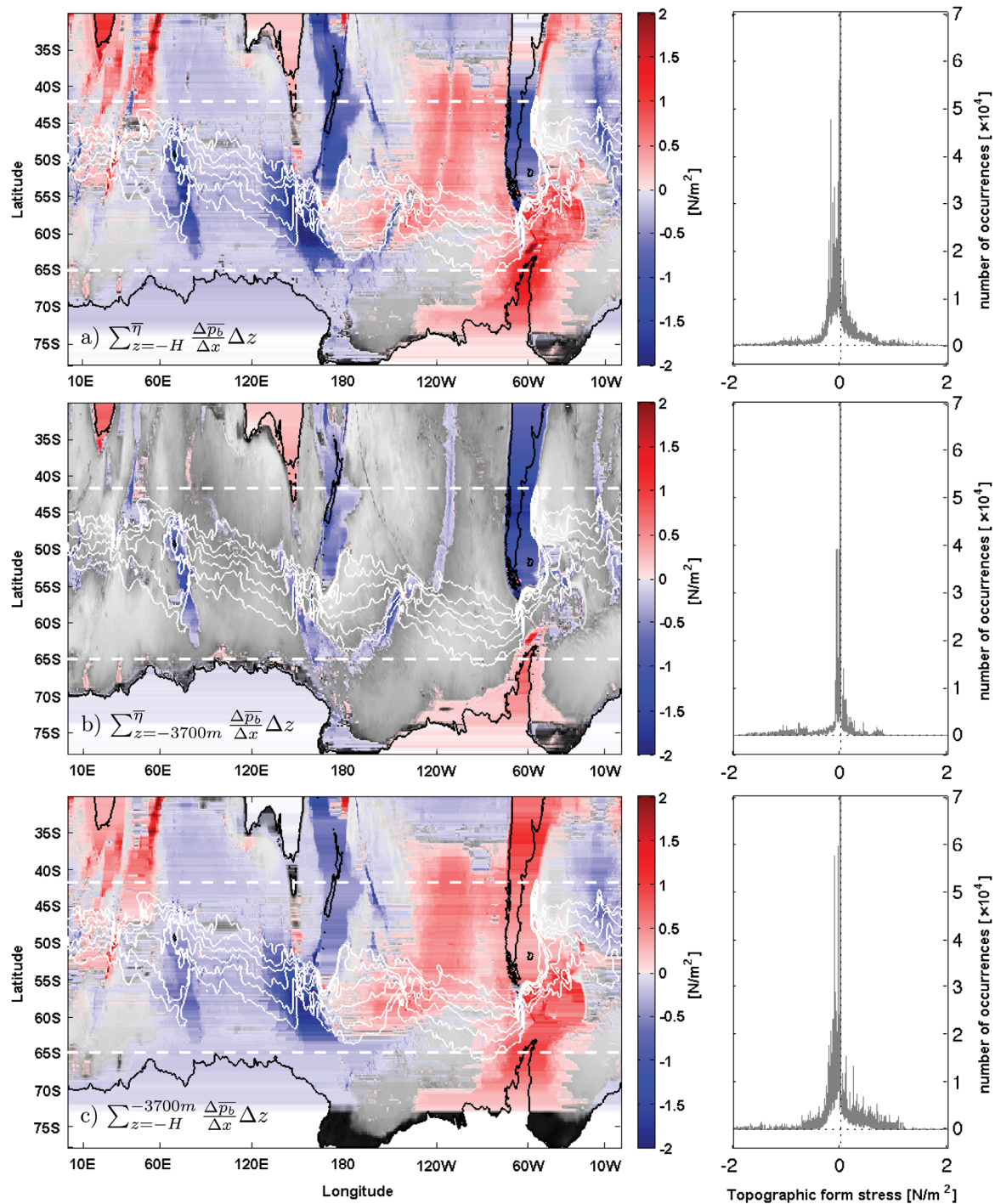


Figure 4. (left) Vertically integrated 6 year time-mean topographic form stress fields and (right) associated histograms, for: (a) full depth, (b) from surface to $z = -3700$ m, and (c) from $z = -3700$ m to seafloor. Solid white lines show SOSE ACC streamlines. Dashed white lines show the limits of the ACC latitudes.

between the Atlantic and Indian gyres result in eastward form stress (Figure 4a, red) across Australia and Africa, respectively. A negative zonal pressure gradient between the Pacific and the Atlantic results in a strong westward form stress (Figure 4a, blue) across South America that extends into the ACC latitudes, discussed in section 4.2.

4.2. Shallow and Deep Contributions to Topographic Form Stress

A few previous studies have noted the presence of two depth regimes in topographic form stress. *Stevens and Ivchenko* [1997] noted two separate “deep” (2056–3874 m) and “very deep” (3874–5499 m) regimes in

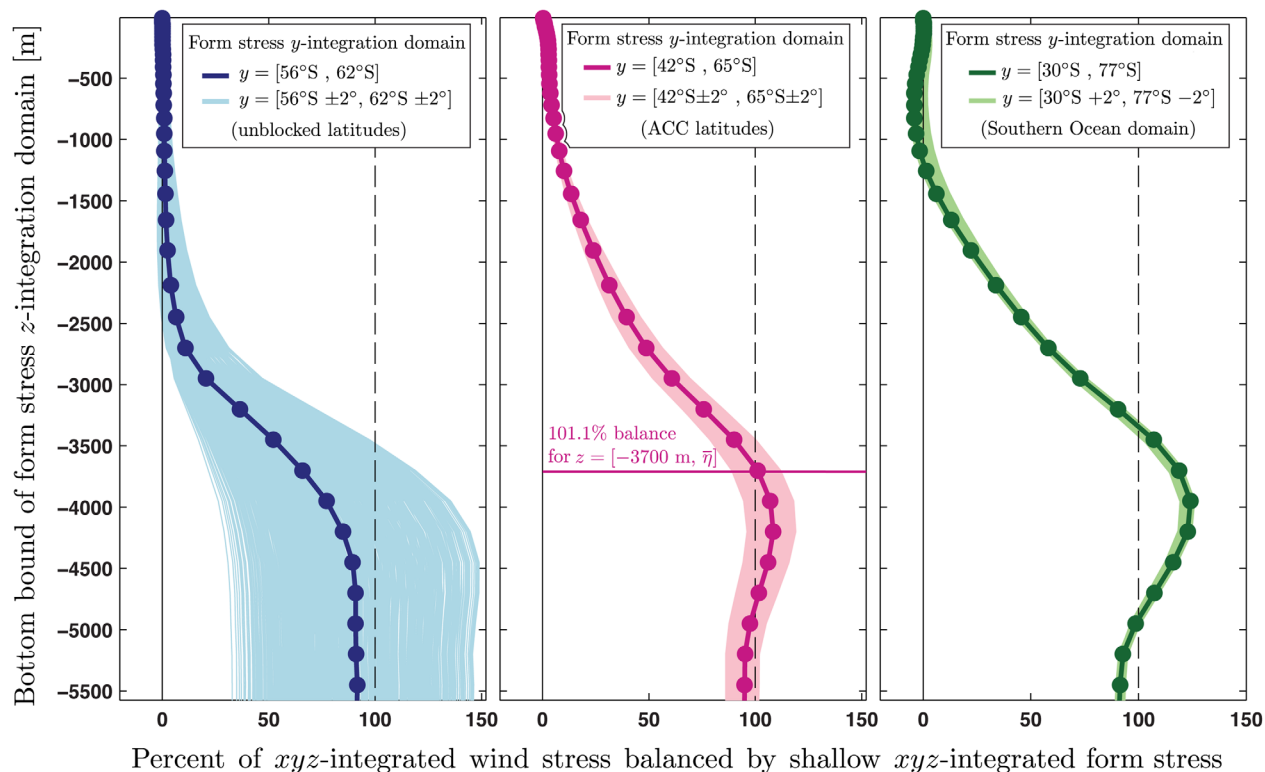


Figure 5. (left) Percent of wind stress balanced by topographic form stress integrated from $z = \bar{\eta}$ to various depths, and over the unblocked latitudes, (middle) the ACC latitudes, and (right) the full Southern Ocean domain. The division between the “shallow” form stress regime and “deep” form stress regime for the ACC latitudes is marked at $z = -3700$ m.

FRAM’s zonal mean topographic form stress signal. In the deep regime, the authors found that topographic form stress was of the same order of magnitude as the wind stress. In the very deep regime, they found that the zonal mean topographic form stress had the same sign as the wind stress—implying an average pressure gradient that would act to accelerate, rather than decelerate the ACC flow—and was an order of magnitude smaller. Grezio *et al.* [2005] noted a similar division in the mean form stress signal between deep (3722–4989 m) and very deep (4989–5500 m) regimes in OCCAM; topographic form stress was of the same order of magnitude as wind stress in the deep regime, but an order of magnitude smaller in the very deep regime. These authors too noted that at some latitudes, the sign of the topographic form stress in the very deep regime was the same as the wind stress.

In SOSE, as well, the integrated topographic form stress can be divided into two regimes: shallower and deeper than 3700 m. Figure 4 shows the vertically integrated topographic form stress field (Figure 4a), along with the shallow regime integrated from the surface to $z = -3700$ m (Figure 4b) and the deep regime from $z = -3700$ m to the seafloor (Figure 4c). The topographic form stress signal integrated from the surface to 3700 m resembles the *Munk and Palmén* paradigm; within the ACC latitudes, primarily westward topographic form stress concentrates over large-scale bottom topography, along with South America. The form stress signal integrated from 3700 m to depth reveals a large-scale structure that tends to cancel in the zonal integral.

For all three fields, the vast majority (>99%) of the individual topographic form stress signals fall between -2 and 2 N/m^2 , an order of magnitude larger than the wind stress signal. Distributions of form stress signals (Figure 4, right) for both the shallow regime and the deep regime are narrowly distributed around their respective means, with a few outliers occurring in regions of very narrow ridges such as Macquarie Ridge, where a very small Δx serves to magnify the pressure difference across the ridge.

The degree to which the shallow regime balances the wind stress varies with both latitudinal and depth bounds (Figure 5). For the full Southern Ocean domain (30°S to 77°S), the shallow form stress regime balances the wind stress with a bottom bound closer to $z = -3300$ m, and shows very little variability when the

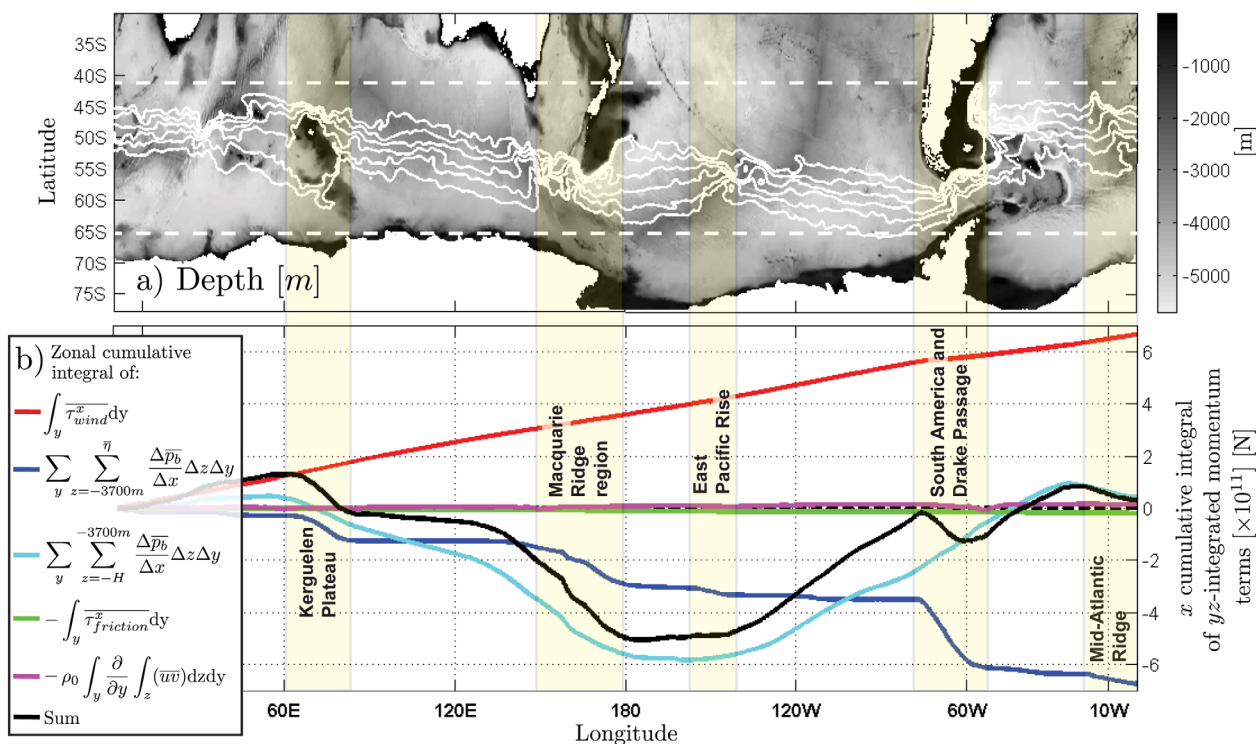


Figure 6. (a) SOSE bathymetry with important regions shaded in yellow, ACC streamlines shown in white, and ACC latitudinal bounds marked by dashed white lines. (b) Zonal cumulative integral of y - z integrated momentum terms between ACC latitudes 42°S and 65°S . Deep topographic form stress (light blue) decreases and then increases, largely canceling in the circumpolar zonal integral. Shallow topographic form stress (dark blue) shows step-like decreases at (from west): Kerguelen Plateau; the Macquarie Ridge region; the East Pacific Rise; South America and the Drake Passage; and the Mid-Atlantic Ridge.

latitudinal bounds are slightly narrowed. For ACC latitudes 42°S to 65°S , the shallow topographic form stress regime bound by $z = [-3700 \text{ m}, \bar{\eta}]$ balances 101% of the wind stress in the total integral. Shallow regimes bound at deeper depths tend to overshoot the wind stress signal, until the balance returns to 100% with a bottom bound of approximately $z = -4500 \text{ m}$, finally reaching 95% of wind stress balanced when the full z domain is included.

For the unbounded latitudes 56°S to 62°S , the balance between shallow form stress and wind stress is relatively poor; only 66% of the wind stress is balanced by a shallow regime bound by $z = [-3700 \text{ m}, \bar{\eta}]$, and only 92% of the wind stressed is balanced when the full z domain is included. Changing the bounds of the latitudinal domain results in significant variability in the amount of wind stress balanced by form stress, ranging from 33% to 146% over the full z domain. This large range reflects the importance of including continents in the form stress calculation; the inclusion of portions of South America and/or the Antarctic Peninsula in the latitudinal domain results in a large variation in the size of the integrated form stress signal.

4.3. Shallow Ridges

Figure 6 reveals the most significant contributors to the shallow topographic form stress signal in the ACC latitudes 42°S to 65°S (Table 2): the cumulative zonal integral takes the shape of a step function that decreases at the ridges that contribute the most to the integrated form stress signal. Table 1 lists these major contributors, and Figure 7 zooms in to their locations. From west, Kerguelen Plateau (Figure 7b) contributes 13% of the total westward form stress in the ACC latitudes; the Southeast Indian Ridge/Macquarie Ridge/Campbell Plateau region (Figure 7c) contributes 20%; the Drake Passage/South America region (Figure 7e) contributes nearly half of the total form stress, at 42%; and there are smaller contributions from the East Pacific Rise (3%; Figure 7d)) and Mid-Atlantic Ridge (4%; not pictured) that are less obvious in the cumulative integral shown in Figure 6.

For most of the ACC's path, only undersea ridges contribute to the shallow topographic form stress signal. Form stress across South America, though, plays a key role in the overall momentum balance in the ACC

Table 2. Principle Contributors to the Shallow Form Stress Signal Over ACC Latitudes 42°S to 65°S

Location	Percent Contributed To Total Westward Shallow Form Stress Signal
Kerguelen Plateau	13%
Southeast Indian Ridge/Macquarie Ridge/Campbell Plateau region	20%
East Pacific Rise	3%
South America and Drake Passage	42%
Mid-Atlantic Ridge	4%

latitudes. Net westward form stress across South America not only dwarfs the form stress across the Drake Passage fracture zones, but constitutes 40% of the total westward topographic form stress signal.

4.4. Deep Density Dipole

The deep regime, dominated by large zonal pressure gradients that span thousands of kilometers, tends to cancel in the zonal integral.

The deep regime depends on pressure differences across deep abyssal ocean basins that are often separated not only by the large shallow ridges, but also by long expanses of deeper plains. The deep form stress signal depends on a zonal dipole in the pressure in these deep abyssal basins: higher pressure in the deep basins underlying the Atlantic and Indian sectors of the Southern Ocean, and lower pressure in the deep basins underlying the Pacific sector (Figure 8). A comparison of deep enclosed basins along a latitudinal circle—Enderby Basin to Amundsen Basin to Weddell Basin, for instance—reveals

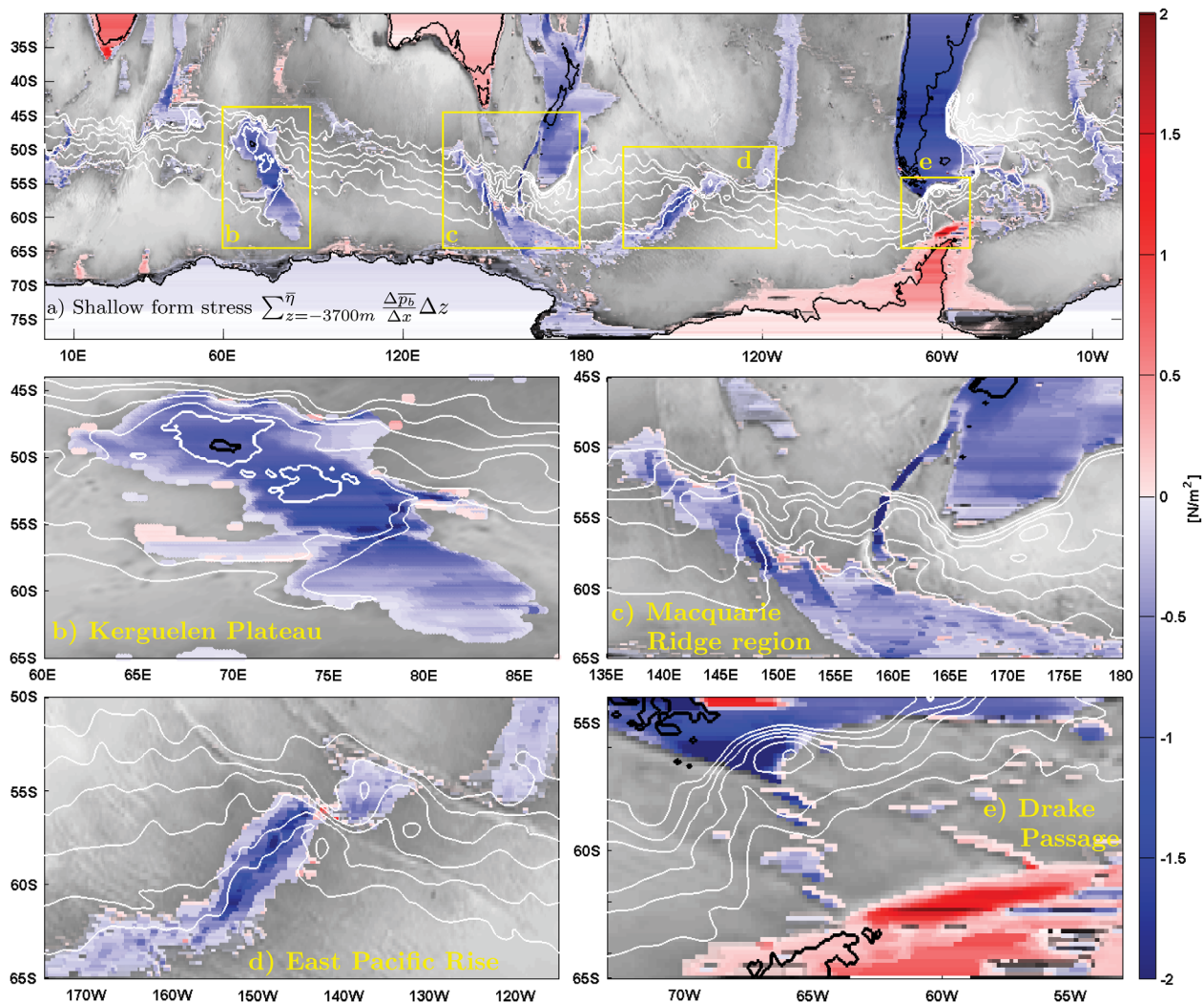


Figure 7. (a) Shallow topographic form stress. Close-up views of: (b) Kerguelen Plateau; (c) Southeast Indian Ridge/Macquarie Ridge/Campbell Plateau region; (d) East Pacific Rise region; and (e) Drake Passage. Solid white lines show SOSE ACC streamlines. Solid black lines show land boundaries.

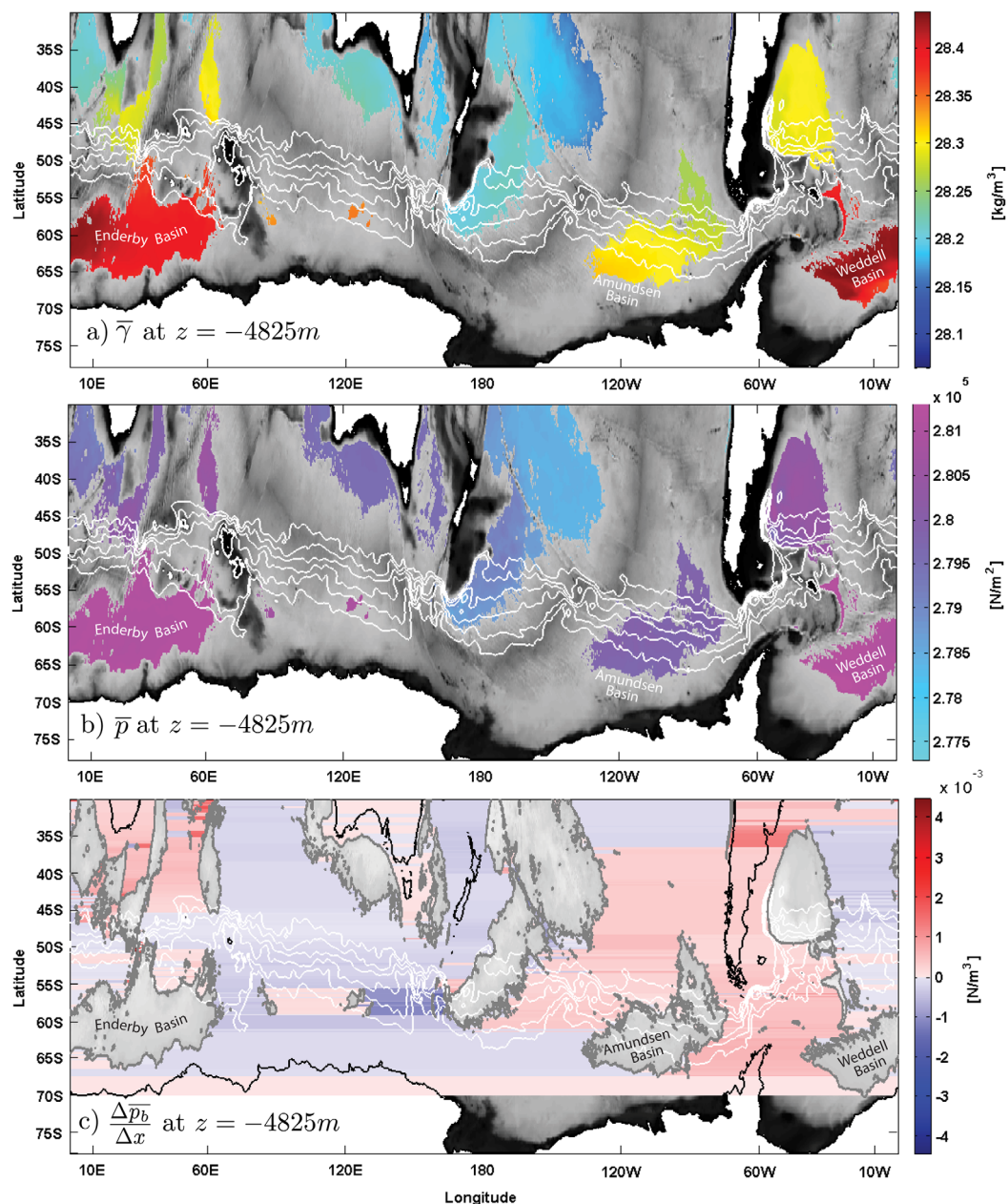


Figure 8. Time-mean map of (a) neutral density, (b) total pressure, and (c) topographic form stress at $z = -4825\text{ m}$. Denser water in the deep Indian and Atlantic sectors results in higher deep basin pressures than in the Pacific sector; thus the deep topographic form stress signal is largely negative between the Indian and Pacific deep basins, and largely positive between the Pacific and Atlantic deep basins.

a denser-lighter-denser pattern of Antarctic Bottom Water (Figure 8a), and an associated pattern of higher-lower-higher deep pressure (Figure 8b).

From the Indian to the Pacific sector, the high-to-low pressure gradient between the deep basins results in westward form stress (Figure 8c, blue) across the deep plains. From the Pacific to the Atlantic sector, the low-to-high pressure gradient between the deep basins results in an eastward form stress (Figure 8c, red) across the plains. This deep density dipole thus creates a deep topographic form stress regime that, regionally, can result in a very large eastward or westward form stress, but largely cancels in the zonal integral.

4.5. Time Variability

Thus far we have focused on the spatial structure of the 6 year time-mean momentum balance only. Integrating the time-varying wind stress and form stress over all longitudes and the ACC latitudes allows us to

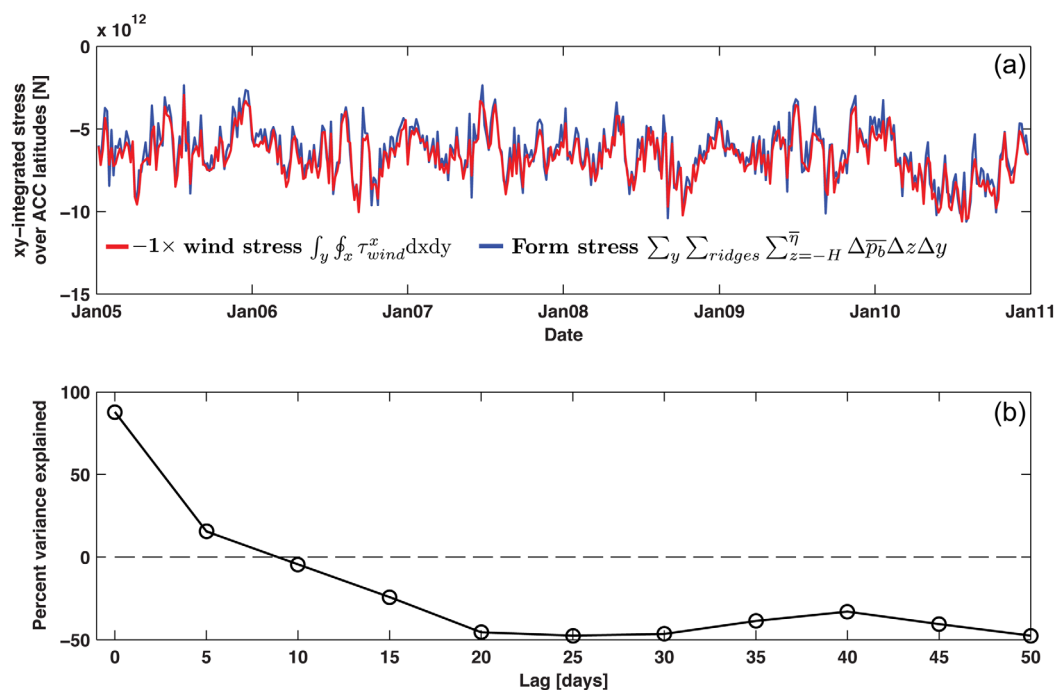


Figure 9. (a) Five day averaged time series of wind stress and topographic form stress integrated over all longitudes and ACC latitudes 42°S to 65°S ; wind stress signal is multiplied by -1 . (b) Percent variance in the topographic form stress signal explained by the wind stress at time lags 0–50 days, over 5 day increments. Maximum of 88% variance explained at 0 lag indicates a rapid topographic form stress response to changes in the wind stress signal.

evaluate the time variability of the overall input and output momentum signals in the ACC. Figure 9a shows the wind stress and topographic form stress 5 day averaged time series, where the wind stress has been inverted to track with the topographic form stress.

There is little lag between the form stress signal and the wind stress signal. The wind stress signal explains 88% of the variance in the form stress signal at zero lag, with a quick drop off below zero variance explained at a 15 day lag (Figure 9b). This high variance explained at zero lag suggests a rapid barotropic response in the ACC system to changes in wind stress, an effect noted by *Hughes et al.* [1999] via comparisons of wind stress and ACC transport, and explored via theoretical and modeling efforts by *Webb and Cuevas* [2006], *Zika et al.* [2013], *Ward and Hogg* [2011], *Thompson and Naveira Garabato* [2014], and others.

Figure 10a shows that the variability in the integrated topographic form stress signal concentrates over topography that lies beneath the ACC fronts. Topography close to the vigorously eddying Agulhas region shows some of the largest standard deviation, along with regions of narrow topography that act as gates across the ACC's path, like Macquarie Ridge and the Drake Passage fracture zones. Even small seamounts and fracture zones in the plains that underly the ACC frontal paths show a high variance, especially in the Indian Ocean between Kerguelen Plateau and the Southeast Indian Ridge. In regions where the ACC flows around—rather than over and through—the barrier, such as the Campbell Plateau and South America, the variance is much lower, even though these regions contribute a large portion of the time-mean zonally integrated form stress signal.

We check that the state estimation procedure is not favorably adjusting the wind stress field over these regions of high form stress variation by mapping the SOSE wind stress adjustment fields—the difference between the ERA-Interim wind stress data and the SOSE wind stress fields at each time step. We find that there is no correlation between the wind stress adjustment fields and the continents or undersea ridges. Instead, adjustment to the ERA-Interim wind stress data in the ACC latitudes are modest and somewhat homogenous (Figure 10b), with SOSE adjustment variance smaller than 5% of the ERA-Interim variance at most locations in the ACC latitudes. Lag correlation between the ERA-Interim wind stress signal and the form stress signal shows that the ERA-Interim wind stress explains 80% of the variance in the form stress

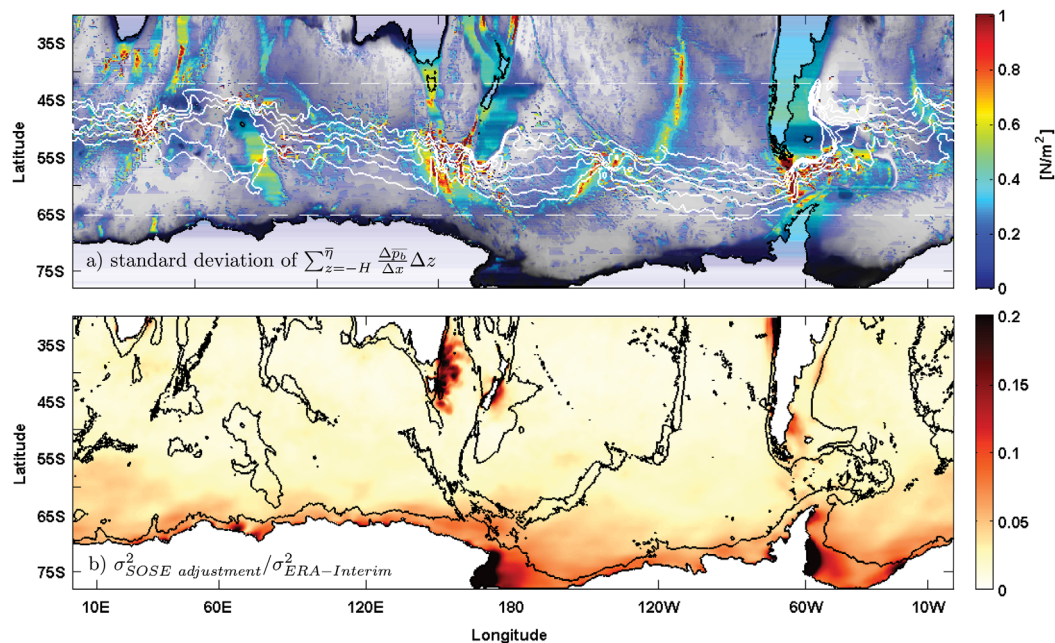


Figure 10. (a) Standard deviation at each point in the topographic form stress field. Higher standard deviation occurs at shallow ridges over which most of the form stress signal is concentrated, and at locations that underlie the path of the ACC jets. (b) Variance of SOSE adjustment to the ERA-Interim wind stress field normalized by the ERA-Interim wind stress variance. The 3000 m topographic contour is shown in black.

signal at zero lag, with a similarly quick drop off below zero variance explained at a 15 day lag. This tells us that a dynamical explanation must underlie this high zero-lag correlation, rather than a result of the modeling process.

5. Conclusions

We have shown that the SOSE momentum balance aligns with previous channel and general circulation model findings: in the zonal integral, topographic form stress acts as the primary balance for wind stress over the Southern Ocean. SOSE's 4-D fields have allowed us to look at the spatial and temporal structure that contributes to this net westward form stress signal, and we can confirm *Munk and Palmén's* [1951] original theory and *Gille's* [1997] finding that the shallow ridges underlying the ACC serve as the primary locations of the westward form drag that balances wind stress.

By mapping the topographic form stress, we have quantified the relative role of the topography that contributes to the overall zonally integrated momentum balance. We find that while the expected submerged ridges do play an important role in the momentum balance, it is South America that plays the most important role, contributing nearly half of the total topographic form stress signal. We also find that the Southeast Indian Ridge contributes to the signal, while the Scotia Arc, located south of much of the ACC flow, and contributes little to the total time-mean form stress signal.

We have also characterized two separate deep and shallow form stress regimes—the shallow, wherein undersea ridges and South America combine to balance the wind stress, and the deep, wherein large local form stresses ultimately balance in the zonal integral. The presence of the deep regime helps to explain the small westward form stress found in the deepest parts of the zonally integrated signal calculated in FRAM [Stevens and Ivchenko, 1997] and OCCAM [Grezio et al., 2005]; these signals are small because they are residuals of two large westward and eastward deep form stress signals, and they are net positive because the positive form stress between the Pacific and the Indo/Atlantic basins slightly outweighs the negative form stress between the Indo/Atlantic and Pacific basins. We attribute this deep basin density dipole to the greater presence of denser Antarctic Bottom Water in the deep Atlantic and Indian basins than in the deep Pacific basins.

Finally, the integrated form stress variance explained by the integrated wind stress signal peaks at time lag less than 5 days, suggesting that changes in the wind stress are translated rapidly down to the level of bottom topography. At the same time, this analysis makes clear that momentum must be carried a significant distance not only vertically, but horizontally as well, before it can exit the ACC system. The mechanisms that transport momentum from source to sink are the focus of our future efforts.

Appendix A: Zonal-Integrated and Depth-Integrated ACC Momentum Balance

Assuming steady state and applying the continuity equation, the time-mean zonal momentum equation can be written:

$$\rho_0 \frac{\partial}{\partial x} (\overline{u\overline{u}}) + \rho_0 \frac{\partial}{\partial y} (\overline{u\overline{v}}) + \rho_0 \frac{\partial}{\partial z} (\overline{u\overline{w}}) - \rho_0 f \overline{v} = -\frac{\partial \overline{p}}{\partial x} + \frac{\partial \overline{\tau^x}}{\partial z} + \rho_0 \eta \nabla^2 \overline{u}, \tag{A1}$$

where (u, v, w) are velocities in the (x, y, z) directions, ρ_0 is background seawater density, f is the Coriolis parameter, p is pressure, τ^x is zonal stress, η is kinematic viscosity, and the overbar indicates the time mean.

Following *Stevens and Ivchenko* [1997], *Johnson and Bryden* [1989], and others, we take the circumpolar zonal integral and the vertical integral from seafloor $z = -H(x,y)$ to sea surface $z = \overline{\eta}(x,y)$, yielding:

$$\begin{aligned} & \rho_0 \oint_x \int_{z=-H}^{z=\overline{\eta}} \underbrace{\left[\frac{\partial}{\partial x} (\overline{u\overline{u}}) + \frac{\partial}{\partial y} (\overline{u\overline{v}}) + \frac{\partial}{\partial z} (\overline{u\overline{w}}) \right]}_A dz dx \\ & = - \oint_x \int_{z=-H}^{z=\overline{\eta}} \frac{\partial \overline{p}}{\partial x} dz dx + \underbrace{\oint_x \int_{z=-H}^{z=\overline{\eta}} \frac{\partial \overline{\tau^x}}{\partial z} dz dx}_B, \end{aligned} \tag{A2}$$

where we have neglected the small integrated Coriolis and interior viscosity terms.

Integrating the flux divergence term (A), we have:

$$\begin{aligned} & \oint_x \int_{z=-H}^{z=\overline{\eta}} \left[\frac{\partial}{\partial x} (\overline{u\overline{u}}) + \frac{\partial}{\partial y} (\overline{u\overline{v}}) + \frac{\partial}{\partial z} (\overline{u\overline{w}}) \right] dz dx = \\ & \oint_x \left[\frac{\partial}{\partial x} \int_{z=-H}^{z=\overline{\eta}} \overline{u\overline{u}} dz - (\overline{u\overline{u}})|_{z=\overline{\eta}} \frac{\partial \overline{\eta}}{\partial x} - (\overline{u\overline{u}})|_{z=-H} \frac{\partial H}{\partial x} \right. \\ & \quad + \frac{\partial}{\partial y} \int_{z=-H}^{z=\overline{\eta}} \overline{u\overline{v}} dz - (\overline{u\overline{v}})|_{z=\overline{\eta}} \frac{\partial \overline{\eta}}{\partial y} - (\overline{u\overline{v}})|_{z=-H} \frac{\partial H}{\partial y} \\ & \quad \left. + (\overline{u\overline{w}})|_{z=\overline{\eta}} - (\overline{u\overline{w}})|_{z=-H} \right] dx. \end{aligned} \tag{A3}$$

The first term on the right-hand side disappears in the circumpolar zonal integral. Noting that $w|_{\overline{\eta}} = u|_{\overline{\eta}} \frac{\partial \overline{\eta}}{\partial x} + v|_{\overline{\eta}} \frac{\partial \overline{\eta}}{\partial y}$, (neglecting Stokes drift) and $w|_{-H} = -u|_{-H} \frac{\partial H}{\partial x} - v|_{-H} \frac{\partial H}{\partial y}$, we rewrite this equation as:

$$\begin{aligned} & \oint_x \int_{z=-H}^{z=\overline{\eta}} \left[\frac{\partial}{\partial x} (\overline{u\overline{u}}) + \frac{\partial}{\partial y} (\overline{u\overline{v}}) + \frac{\partial}{\partial z} (\overline{u\overline{w}}) \right] dz dx = \\ & \oint_x \left[-(\overline{u\overline{u}})|_{z=\overline{\eta}} \frac{\partial \overline{\eta}}{\partial x} - (\overline{u\overline{u}})|_{z=-H} \frac{\partial H}{\partial x} \right. \\ & \quad + \frac{\partial}{\partial y} \int_{z=-H}^{z=\overline{\eta}} \overline{u\overline{v}} dz - (\overline{u\overline{v}})|_{z=\overline{\eta}} \frac{\partial \overline{\eta}}{\partial y} - (\overline{u\overline{v}})|_{z=-H} \frac{\partial H}{\partial y} \\ & \quad \left. + (\overline{u\overline{u}})|_{z=\overline{\eta}} \frac{\partial \overline{\eta}}{\partial x} + (\overline{u\overline{v}})|_{z=\overline{\eta}} \frac{\partial \overline{\eta}}{\partial y} + (\overline{u\overline{u}})|_{z=-H} \frac{\partial H}{\partial x} + (\overline{u\overline{v}})|_{z=-H} \frac{\partial H}{\partial y} \right] dx. \end{aligned} \tag{A4}$$

Canceling terms, the final form for the vertically and zonally integrated flux divergence term is simply:

$$\oint_x \frac{\partial}{\partial y} \int_{z=-H}^{\bar{\eta}} (\overline{uv}) dz dx \quad (A5)$$

We now expand the stress term (B) into wind stress at the surface of the fluid, τ_{wind}^x , and frictional stress at the bottom and sidewalls of the fluid, $\tau_{friction}^x$. Evaluating the depth integral, this term becomes:

$$\oint_x \int_{z=-H}^{\bar{\eta}} \frac{\partial \overline{\tau^x}}{\partial z} dz dx = \oint_x [\overline{\tau_{wind}^x} - \overline{\tau_{friction}^x}] dx. \quad (A6)$$

Combining terms (A) and (B) with the pressure gradient term, we have the time-mean zonally and vertically integrated zonal momentum equation:

$$\rho_0 \oint_x \frac{\partial}{\partial y} \int_{z=-H}^{\bar{\eta}} \overline{uv} dz dx = - \oint_x \int_{z=-H}^{\bar{\eta}} \frac{\partial \overline{p}}{\partial x} dz dx + \oint_x \overline{\tau_{wind}^x} dx - \oint_x \overline{\tau_{friction}^x} dx. \quad (A7)$$

Acknowledgments

SOSE data are available at sose.ucsd.edu. This work was supported by National Science Foundation grants PLR-1141922 and PLR-0961218. J. Masich was also supported by the Department of Defense through the National Defense Science and Engineering Graduate Fellowship Program. M. R. Mazloff acknowledges the NSF for support of this research through grants OCE-1234473 and PLR-1425989. SOSE was produced using the Extreme Science and Engineering Discovery Environment (XSEDE), which is supported by NSF grant number MCA06N007. Thanks to Sarah Gille and C. S. Jones for useful discussion, and to two anonymous reviewers for their insightful comments.

References

- Böning, C. W., A. Disper, M. Visbeck, S. R. Rintoul, and F. U. Schwarzkopf (2008), The response of the Antarctic Circumpolar Current to recent climate change, *Nat. Geosci.*, *1*(12), 864–869, doi:10.1038/ngeo362.
- Gille, S. T. (1997), The Southern Ocean momentum balance: Evidence for topographic effects from numerical model output and altimeter data, *J. Phys. Oceanogr.*, *27*(10), 2219–2232, doi:10.1175/1520-0485(1997)027<2219:TSOMBE>2.0.CO;2.
- Grezio, A., N. C. Wells, V. O. Ivchenko, and B. A. de Cuevas (2005), Dynamical budgets of the Antarctic Circumpolar Current using ocean general-circulation models, *Q. J. R. Meteorol. Soc.*, *131*(607), 833–860, doi:10.1256/qj.03.213.
- Holloway, G. (1987), Systematic forcing of large-scale geophysical flows by eddy-topography interaction, *J. Fluid Mech.*, *184*(–1), 463–476, doi:10.1017/S0022112087002970.
- Howard, E., A. McC. Hogg, S. Waterman, and D. P. Marshall (2015), The injection of zonal momentum by buoyancy forcing in a Southern Ocean model, *J. Phys. Oceanogr.*, *45*(1), 259–271, doi:10.1175/JPO-D-14-0098.1.
- Hughes, C. W., M. P. Meredith, and K. J. Heywood (1999), Wind-driven transport fluctuations through drake passage: A Southern mode, *J. Phys. Oceanogr.*, *29*(8), 1971–1992, doi:10.1175/1520-0485(1999)029<1971:WDTFTD>2.0.CO;2.
- Ivchenko, V., K. Richards, and D. Stevens (1996), The dynamics of the Antarctic Circumpolar Current, *J. Phys. Oceanogr.*, *26*, 753–774, doi:10.1175/1520-0485(1996)026<0753:TDOTAC>2.0.CO;2.
- Johnson, G. C., and H. L. Bryden (1989), On the size of the Antarctic Circumpolar Current, *Deep Sea Res., Part A*, *36*(1), 39–53, doi:10.1016/0198-0149(89)90017-4.
- Killworth, P. D., and M. M. Nanneh (1994), Isopycnal momentum budget of the Antarctic Circumpolar Current in the fine resolution Antarctic model, *J. Phys. Oceanogr.*, *24*(6), 1201–1223, doi:10.1175/1520-0485(1994)024<1201:IMBOTA>2.0.CO;2.
- Marshall, J., D. Olbers, H. Ross, and D. Wolf-Gladrow (1993), Potential vorticity constraints on the dynamics and hydrography of the Southern Ocean, *J. Phys. Oceanogr.*, *23*(3), 465–487, doi:10.1175/1520-0485(1993)023<0465:PVCOTD>2.0.CO;2.
- Mazloff, M. R., P. Heimbach, and C. Wunsch (2010), An eddy-permitting Southern Ocean state estimate, *J. Phys. Oceanogr.*, *40*(5), 880–899, doi:10.1175/2009JPO4236.1.
- McWilliams, J. C., W. R. Holland, and J. H. Chow (1978), A description of numerical Antarctic circumpolar currents, *Dyn. Atmos. Oceans*, *2*(3), 213–291, doi:10.1016/0377-0265(78)90018-0.
- Munk, W. H., and E. Palmén (1951), Note on the dynamics of the Antarctic Circumpolar Current, *Tellus*, *3*(1), 53–55, doi:10.1111/j.2153-3490.1951.tb00776.x.
- Olbers, D. (1998), Comments on “On the obscurantist physics of form drag in theorizing about the circumpolar current,” *J. Phys. Oceanogr.*, *28*(8), 1647–1654, doi:10.1175/1520-0485(1998)028<1647:COOTOP>2.0.CO;2.
- Olbers, D., D. Borowski, C. Völker, and J.-O. Wölf (2004), The dynamical balance, transport and circulation of the Antarctic Circumpolar Current, *Antarct. Sci.*, *16*(04), 439–470.
- Stevens, D. P., and V. O. Ivchenko (1997), The zonal momentum balance in an eddy-resolving general-circulation model of the Southern Ocean, *Q. J. R. Meteorol. Soc.*, *123*(540), 929–951.
- Swart, N. C., and J. C. Fyfe (2012), Observed and simulated changes in the Southern Hemisphere surface westerly wind-stress, *Geophys. Res. Lett.*, *39*, L16711, doi:10.1029/2012GL052810.
- Thompson, A. F., and A. C. Naveira Garabato (2014), Equilibration of the Antarctic Circumpolar Current by standing meanders, *J. Phys. Oceanogr.*, *44*(7), 1811–1828, doi:10.1175/JPO-D-13-0163.1.
- Thompson, D. W. J., and S. Solomon (2002), Interpretation of Recent Southern Hemisphere Climate Change, *Science*, *296*(5569), 895–899, doi:10.1126/science.1069270.
- Treguier, A. M., and J. C. McWilliams (1990), Topographic influences on wind-driven, stratified flow in a β -plane channel: An idealized model for the Antarctic Circumpolar Current, *J. Phys. Oceanogr.*, *20*(3), 321–343, doi:10.1175/1520-0485(1990)020<0321:TLOWDS>2.0.CO;2.
- Ward, M. L., and A. M. Hogg (2011), Establishment of momentum balance by form stress in a wind-driven channel, *Ocean Modell.*, *40*(2), 133–146, doi:10.1016/j.ocemod.2011.08.004.
- Webb, D. J., and B. A. D. Cuevas (2006), On the fast response of the Southern Ocean to changes in the zonal wind, *Ocean Sci. Discuss.*, *3*(3), 471–501.
- Wolff, J.-O., E. Maier-Reimer, and D. J. Olbers (1991), Wind-driven flow over topography in a zonal β -plane channel: A quasi-geostrophic model of the Antarctic Circumpolar Current, *J. Phys. Oceanogr.*, *21*(2), 236–264, doi:10.1175/1520-0485(1991)021<0236:WDFOTI>2.0.CO;2.
- Zika, J. D., et al. (2013), Vertical eddy fluxes in the Southern Ocean, *J. Phys. Oceanogr.*, *43*(5), 941–955, doi:10.1175/JPO-D-12-0178.1.